THE JOURNAL OF PHYSICAL CHEMISTRY C

pubs.acs.org/JPCC Article

Surface-Energy Control and Characterization of Nanoparticle Coatings

David J. H. Cant,* Caterina Minelli, Katia Sparnacci, Anja Müller, Henryk Kalbe, Michael Stöger-Pollach, Wolfgang E. S. Unger, Wolfgang S. M. Werner, and Alexander G. Shard

Cite This: J. Phys. Chem. C 2020, 124, 11200−11211 Read Online

ACCESS | Metrics & More | Article Recommendations | Supporting Information

ABSTRACT: Accurate and reproducible measurement of the structure and properties of high-value nanoparticles is extremely important for their commercialization. A significant proportion of engineered nanoparticle systems consist of some form of nominally core−shell structure, whether by design or unintentionally. Often, these do not form an ideal core−shell structure, with typical deviations including polydispersity of the core or shell, uneven or incomplete shells, noncentral cores, and others. Such systems may be created with or without intent, and in either case an understanding of the conditions for formation of such particles is desirable. Precise determination of the structure, composition, size, and shell thickness of such particles can prove challenging without the use of a suitable range of characterization techniques. Here, the authors present two such polymer core−shell nanoparticle systems, consisting of polytetrafluoroethylene cores coated with a range of thicknesses of either polymethylmethacrylate or polystyrene. By consideration of surface energy, it is shown that these particles are expected to possess distinctly differing coating structures, with the polystyrene coating being incomplete. A comprehensive characterization of these systems is demonstrated, using a selection of complementary techniques including scanning electron microscopy, scanning transmission electron microscopy, thermogravimetric analysis, dynamic light scattering, differential centrifugal sedimentation, and X-ray photoelectron spectroscopy. By combining the results provided by these techniques, it is possible to achieve superior characterization and understanding of the particle structure than could be obtained by considering results separately.

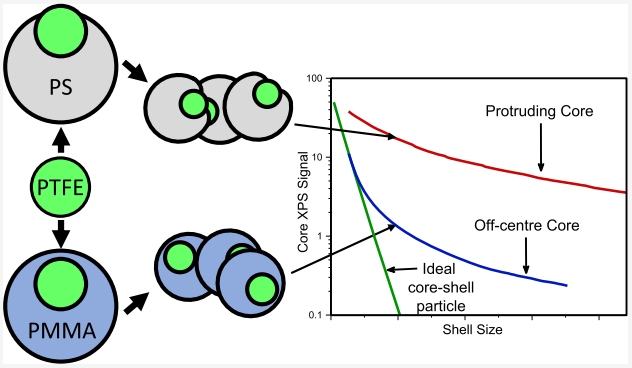

INTRODUCTION

The study of nanoparticle structure and chemistry is of increasing importance for modern technology. Core−shell nanoparticles are now incorporated into a multitude of products with many applications ranging from biomedical imaging, to catalysis, to lighting, and displays. The addition of a shell to a nanoparticle can greatly affect its performance for a variety of reasons: for example in pharmaceuticals, shells with a specific chemistry are used to prevent unspecific protein adsorption and provide targeting functionalities for a variety of therapeutic and diagnostic purposes;[1−5] in catalysis, organic coatings can provide chemoselectivity and efficiency;[6] and in optoelectronic applications, shell properties can impact on charge transport and recombination times.[7−9] As the potential applications for such nanoparticle systems are developed, more complex and specially tailored nanoparticle systems are required. Deviations from the idealized uniform, concentric, spherical core−shell system are common, whether intended or not. Many varieties of nanoparticle structures are in use and development, ranging from particles with incomplete or asymmetric shells,[10,11] to multicore particles,[12] "Janus" particles,[13−15] and others. Understanding the methods by which such morphologies arise during synthesis and methods by which they may be characterized is thus highly valuable. However, accurate identification of the structure and composition of a nonstandard core−shell system is not straightforward because a single characterization technique cannot accurately or representatively determine every structural or compositional parameter. Therefore, it is important to use a range of appropriate methods to properly measure the features of interest of a nanoparticle system. Likewise, control over the creation of such morphologies may be difficult to attain.

Techniques currently used in the characterization and creation of nanoparticles are many and varied.[16−20] It is

Received: March 11, 2020
Revised: April 27, 2020
Published: April 28, 2020

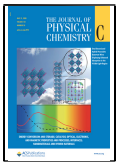

https://dx.doi.org/10.1021/acs.jpcc.0c02161
J. Phys. Chem. C 2020, 124, 11200−11211

common for researchers to focus on selected techniques which target properties of interest. This approach risks a partial or sometimes erroneous understanding of the system under study. This can inhibit reproducibility and further development toward practical implementation of the technology.[21−23] It is therefore important to be aware of these features and be able to measure them in a representative manner. Understanding the ways in which nanoparticle morphology and structure may be controlled is likewise similarly important for the development of high-value and next-generation nanoparticle-based technologies. For liquid-based syntheses of polymer particles, interfacial energy has been shown to play a significant role in the determination of the nanoparticle shape.[24]

In this paper, we present the synthesis and analysis of two similar types of core−shell nanoparticle systems using a range of techniques, including scanning electron microscopy (SEM), scanning transmission electron microscopy (STEM), thermogravimetric analysis (TGA), dynamic light scattering (DLS), differential centrifugal sedimentation (DCS), and X-ray photoelectron spectroscopy (XPS). The two types of nanoparticle systems discussed here are formed of a polytetrafluoroethylene (PTFE) core, coated with varying thicknesses of either polymethylmethacrylate (PMMA) or polystyrene (PS). Both systems form nominally core−shell structures but have distinctly different distributions of shell material around the core due to the differing interfacial energies of the core/shell/water system during synthesis. Nonideal structures are not uncommon for particles made from these materials,[25] thus it is necessary to select characterization techniques with care to ensure confidence in the interpretation of their results.

MATERIALS AND METHODS

The PTFE−PMMA and PTFE−PS core−shell nanoparticles were synthesized by emulsifier-free batch seeded emulsion polymerization in the presence of PTFE seed particles. The employed PTFE suspension (Hyflon MFA 100 LS latex) was supplied by Solvay Specialty Polymers.[25] It consists of a special grade of a perfluoroalkoxy polymer resulting from the polymerization of tetrafluoroethylene and perfluoro(methyl vinyl ether). All of the polymerizations were carried out in a 1 L five neck jacketed reactor at 75 °C equipped with a condenser, a mechanical stirrer, a thermometer, and inlets for nitrogen and monomers. The appropriate amount of PTFE latex was introduced into the reactor containing 500 mL of deionized water at room temperature with a stirring rate of 300 rpm. The mixture was purged with nitrogen, and nitrogen was flowed during the entire polymerization procedure. The mixture was then heated to 80 °C, and the appropriate amount of monomer was added (see Table 1). After an additional 15 min equilibration time, a potassium persulfate aqueous solution (10 mL, 0.74 mmol) was added and the mixture was reacted for 24 h. The obtained latex was purified by dialyses against deionized water (M_w cutoff 14,000 Da). Water was replaced every 12 h for 10 days to eliminate any impurities and unreacted monomers. All of the core−shell lattices were obtained following the above general procedure by varying the initial PTFE latex and monomer amount.

Samples with a PS shell are designated "PTFE−PS" and particles with a PMMA shell are designated "PTFE−PMMA". These two systems were chosen for comparison as calculation of the expected interfacial energies indicated that the PS coating of the PTFE−PS particles should not fully wet the PTFE cores, whereas the PMMA coating of the PTFE−PMMA particles should form a complete coating. This is supported by prior work indicating that the PTFE−PS particles do not have an ideal core−shell morphology.[25]

Table 1. Fractional Mass of PTFE Estimated from the Amount of Monomer Used in the Initial Reaction (Feed) and Measured by TGA

sample	% PTFE feed w/w	% PTFE (TGA) w/w
PTFE−PS(1)	46.5	47.4
PTFE−PS(2)	34.2	34.7
PTFE−PS(3)	27.1	27.2
PTFE−PS(4)	13.7	14.5
PTFE−PS(5)	7.3	7.9
PTFE−PS(6)	3.6	3.8
PTFE−PMMA(1)	33.5	33.5
PTFE−PMMA(2)	17.1	16.3
PTFE−PMMA(3)	7.2	6.8
PTFE−PMMA(4)	3.5	3.3

TGA was performed with a Mettler-Toledo TGA/SDTA851e at a scanning rate of 10 °C/min from room temperature up to 800 °C under nitrogen flow. The analysis was performed on a dried sample obtained by placing 5 mL of the particle suspension in a vacuum oven at 60 °C for 16 h.

DLS is commonly used to measure the size and size distribution of nanoparticles from fluctuations in the intensity of scattered light from particles in suspension. The fluctuations in intensity caused by Brownian motion may be analyzed to provide the hydrodynamic diameter of the particles. DLS of the samples was performed at 25 °C, with a Malvern Zetasizer Nano ZS at the noninvasive backscatter angle of 173°, using a 4 mV He−Ne laser (633 nm). The samples were diluted to the optimal concentration for measurement with ultrapure water. The diameters reported are the *Z*-averages resulting from cumulant analysis, modeling the particles as perfect rigid spheres of known homogeneous density and applying Mie's theory.[26,27] Measurements were performed in triplicate and reported as the zeta-average from cumulant analysis with associated polydispersity index (PI) widths as determined by Malvern Zetasizer software.

DCS measurements were performed with CPS disk centrifuge instruments, model DC24000 (CPS Instruments, Prairieville, LA, USA). Prior to the measurements, a sucrose (Amresco LLC, OH, USA) gradient was built within the disc, according to manufacturer's instructions and allowed to equilibrate for 30 min. Sedimentation measurements were calibrated using polyvinyl chloride particles of nominal size 239 nm and density 1.385 g/cm^3 provided by the manufacturer. The samples were diluted to the optimal concentration for measurement using ultrapure water as the diluent. Measurements were performed at a rotational speed of 24,000 rpm, using a photodetector at a fixed radius opposite a diode laser with a wavelength of 405 nm. Injection volume was set to 100 μL. Particles are detected by a drop in light intensity as they pass through the detection region. The sedimentation time (time from injection to detection) is converted into a particle diameter using the Stokes−Einstein equation[28] and the light absorbance converted into a particle mass at each diameter using Mie's theory. Particles are modeled as perfect spheres of known homogeneous density.

Particle size measurements were performed by SEM measurements in transmission mode using a Zeiss Supra 40 SEM equipped with a high-resolution cathode (Schottky field

https://dx.doi.org/10.1021/acs.jpcc.0c02161
J. Phys. Chem. C 2020, 124, 11200−11211

emitter) and using a dedicated sample holder in combination with the available secondary detector as described in detail elsewhere.[29] The image processing software ImageJ 1.52e was applied for further analysis of the SEM micrographs.[30]

To prepare samples of the PTFE cores for SEM, the original suspension was diluted with ultrapure water by a factor of 10,000. The suspension was filtered using a syringe filter purchased from General Electric Healthcare (Chicago, USA) with a fiberglass membrane and a pore size of 1.2 μm. A 6−10 nm thick carbon film on a 3.05 mm diameter and 10−12 μm thick copper transmission electron microscopy grid of 200 lines/inch purchased from PLANO GmbH (Wetzlar, Germany) was purified for 30 min in a UV/Ozone cleaner. A 5 μL drop was applied onto the carbon film of the copper grid and spin coated. The following spin-coating program was applied: step (1) acceleration with 500 rpm/s up to 1000 rpm kept for 10 s, step (2) acceleration with 500 rpm/s up to 5000 rpm kept for 10 s, step (3) acceleration with 500 rpm/s up to 10,000 rpm kept for 1 min.

To prepare samples of the coated particles for SEM, the original suspensions were diluted with ultrapure water by a factor of 1000 in the case of PTFE−PS(2) and by a factor of 50 in the case of all other samples. The suspensions were filtered using the same kind of syringe filter previously described. A 2 μL drop was applied onto the same kind of copper transmission electron microscopy grid previously described.

STEM was performed on the PTFE−PMMA(1) nanoparticles only. Samples for STEM experiments were deposited onto copper grids with a carbon support film by drop-casting and immediately dried under vacuum in the load-lock of the microscope. STEM experiments were performed using a FEI Tecnai F20 instrument at 200 kV acceleration voltage supplying 0.358 nA beam current. Images were taken in both annular bright field (ABF) and high-angle annular dark field (HAADF) modes. Energy-dispersive X-ray (EDX) spectroscopy measurements were also performed, using an AMETEK Apollo XII detector. EDX data were processed using the software Gatan DigitalMicrograph.[31]

Samples for analysis by XPS were deposited on silicon wafer by drop-casting in a vacuum desiccator. It is important to achieve as uniform and thick coverage of the sample on the substrate as possible when preparing samples for XPS, particularly when quantification of carbon is required, in order to minimize the contribution to the signal from adventitious carbon on the substrate itself.[32] Samples were analyzed with a Kratos Axis Ultra using an Al Kα source (1486.7 eV). Survey spectra were taken from all samples at a pass energy of 160 eV, and higher resolution spectra for the carbon, fluorine, and oxygen 1s peaks were taken at a pass energy of 20 eV.

Theoretical Model for Interfacial Energies. Interfacial energies were estimated by the method of Good and Girifalco,[33] in which the surface energy of a material, σ, is separated into polar (P) and dispersive (D) components and the interfacial energy between two phases A and B calculated according to eq 1.

$$\sigma_{AB} = \sigma_A + \sigma_B - 2\left(\sqrt{\sigma_A^D \sigma_B^D} + \sqrt{\sigma_A^P \sigma_B^P}\right) \quad (1)$$

Values for the surface energy components were acquired from various sources: the values used for PMMA and water were obtained from Carré,[34] while PS and PTFE were assumed to have no polar component, although there is general disagreement in the literature and available online databases on this point. Because of the uncertainty in the actual values, we have used Zisman's values of the critical spreading tension for the dispersive component.[35] The spreading coefficient of a polymer (A) on PTFE (F), S_{AF}, in water (W) is calculated using eq 2.[36]

$$S_{AF} = \sigma_{FW} - (\sigma_{AW} + \sigma_{AF}) \quad (2)$$

If the spreading parameter is negative, then the polymer will not spread on PTFE in water and will form an equilibrium contact angle, θ_E, which can be calculated from Young's relation. The input data and results of these calculations (provided in the Supporting Information in Table S1) indicate that PMMA will spread on PTFE in water, but PS should not. We note there is considerable uncertainty in the contact angle of PS on PTFE in water. If we use various sources of data for the surface energies of polymers, it could be as high as 30° or, in some cases, it should spread on PTFE. Because our observation is that it does not spread on PTFE, we have taken the value calculated in the Supporting Information (20°) for the illustration of expected nanoparticle morphologies. The PMMA coating should completely cover the PTFE core, but other than the requirement to have a complete wetting layer of a few nanometers, the core may be located at any point within the nanoparticle. PS-coated particles, in contrast, have a defined location for the PTFE core because it must touch the surface of the nanoparticle (see Scheme 1).

Scheme 1. (A) Indicative Schematic of the Idealized Morphology of the PTFE Core and PS Shell Particles in Suspension in Water; The Triple Line is Marked with an Arrow Indicating the Contact Angle of PS on PTFE in Water; (B) Schematic of the Morphology of Particles after the Core has Shrunk During Analysis in an Electron Microscope; (C) Schematic Close-Up of the Particle Surface, Describing the "6 nm Core Protrusion" Model Shown Alongside the XPS Data from the PS-Coated Particles in Figure 6—Note This Model Uses a Fixed Protrusion, and As Such the Contact Angle Will Vary With Particle Size; (D) Schematic Close-Up of the Particle Surface Describing the "Core 3 nm below the Surface" Model Shown Alongside the XPS Data From the PMMA-Coated Particles in Figure 6

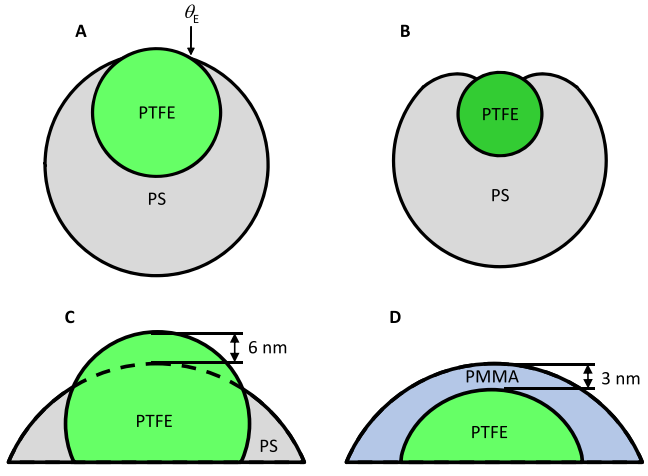

https://dx.doi.org/10.1021/acs.jpcc.0c02161
J. Phys. Chem. C 2020, 124, 11200−11211

Table 2. Average Diameters (D_{DLS}) and PI Widths ($Width_{DLS}$) as Measured by DLS, Average Particle Densities, and Associated Uncertainties as Determined by DCS (ρ_{DCS}), and Estimated Shell-Thicknesses Obtained from Combining the TGA, DCS, and DLS Results (T_{bulk})

sample	D_{DLS} (nm)	PI $width_{DLS}$ (nm)	ρ_{DCS} (g/cm^3)	T_{bulk} (nm)
cores	49 ± 1	29 ± 1		N/A
PTFE−PS(1)	63.1 ± 0.9	15.0 ± 0.5	1.25 ± 0.25	8.0
PTFE−PS(2)	71.1 ± 0.1	13 ± 2	1.17 ± 0.23	12.0
PTFE−PS(3)	84.4 ± 0.4	12 ± 3	1.11 ± 0.22	18.5
PTFE−PS(4)	98 ± 1	14 ± 6	1.09 ± 0.22	25.5
PTFE−PS(5)	120 ± 1	21 ± 3	1.07 ± 0.21	36.5
PTFE−PS(6)	159 ± 2	14 ± 4	1.06 ± 0.21	56.0
PTFE−PMMA(1)	72.8 ± 0.9	15 ± 1	1.27 ± 0.25	13.0
PTFE−PMMA(2)	93.7 ± 0.9	20 ± 3	1.22 ± 0.24	23.5
PTFE−PMMA(3)	122.7 ± 0.9	25 ± 5	1.18 ± 0.24	38.0
PTFE−PMMA(4)	160 ± 2	26 ± 8	1.17 ± 0.23	56.5

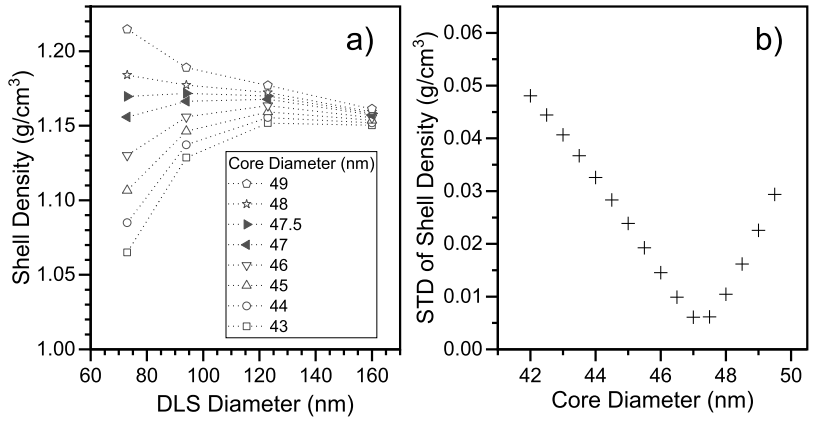

Figure 1. (a) Plot of calculated PMMA shell densities against DLS diameter for a range of nominal core diameters and (b) plot of standard deviations of the calculated densities for all PTFE−PMMA particle sizes at each nominal core diameter.

RESULTS AND DISCUSSION

Bulk Analysis. In the thermograms for both the PTFE−PS and PTFE−PMMA particles (given in the Supporting Information, Figure S1), there are two main mass losses. The lower temperature mass loss is associated with the degradation of the shell-forming polymers which occurs at 410 °C (midpoint) for PS and at 350 °C for PMMA. The mass loss at 570 °C corresponds to PTFE decomposition. The average particle composition is thus determined from the remaining mass after the initial loss of the shell material. These compositions provide good agreement with those expected from the initially added amounts of PTFE and monomer and are given in Table 1.

The particle diameters (D_{DLS}) measured by DLS and densities (ρ_{DCS}) calculated from DCS results are reported in Table 2. It should be noted that DCS measures the Stokes' diameter, which is equivalent to the hydrodynamic diameter measured by DLS for the case of spherical particles. These diameters would therefore be expected to be slightly larger than sizes as measured using physical techniques such as electron microscopy or XPS.

The excellent size resolution provided by DCS demonstrates a relatively monodisperse size distribution, the exceptions being the PTFE−PMMA(4) population where minor populations of doublets (i.e., two particles agglomerated together) and triplets can be seen, and the PTFE cores which were too aggregated for measurement (DCS size distributions are given in Figure S2 of the Supporting Information). This observation of monodisperse populations means that the diameters measured by DLS should be accurate if the particles are also spherical, the exceptions being PTFE−PMMA(4) in which clear aggregate peaks were observed by DCS and the PTFE cores which were too aggregated for reliable measurement by DCS. Therefore, the diameters measured by DLS for those particles will be larger than the primary particle diameter.

In DCS measurements, the sedimentation time depends on both the size and density of the particles. If the size is known from an independent technique, such as DLS, DCS can be used to measure the average density of the particles by modeling them as perfect homogeneous spheres. Combining the DCS, DLS, and TGA results can further allow estimation of both core and shell densities using an assumed core diameter. Comparing the results obtained in this manner for multiple particle types across multiple assumed core diameters can then also be used to provide a refined estimate for the core diameter and thus the shell thickness.

First, we can determine the average mass of the shell, M_{shell}, and likewise the core, M_{core}, in a particle by combining the measured particle densities with the fractional mass of the shell and core material determined by TGA, f_{shell}, and f_{core} respectively, as shown in eq 3.

$$M_{shell} = \left(\rho_{DCS}\frac{\pi}{6}{D_{DLS}}^3\right)f_{shell} \quad (3)$$

The core and shell densities are thus given by eqs 4 and 5, assuming an ideal core−shell structure. This will also be valid

https://dx.doi.org/10.1021/acs.jpcc.0c02161
J. Phys. Chem. C 2020, 124, 11200−11211

for a nonideal case in which the diameters used are interpreted as the diameters for volume-equivalent spheres.

$$\rho_{\text{shell}} = \frac{M_{\text{shell}}}{\frac{\pi}{6}(D_{\text{DLS}}{}^3 - D_{\text{core}}{}^3)} \quad (4)$$

$$\rho_{core} = \frac{M_{\text{core}}}{\frac{\pi}{6}(D_{\text{core}}{}^3)} \quad (5)$$

If we assume that the core volume is constant irrespective of particle size, then the core diameter can be altered in eqs 4 and 5 to extract the associated shell density for each population. We expect that the shell density should be constant for all particles and close to that of bulk PMMA, which is ∼1.18 g/cm^{-3} for atactic PMMA.[37] Using the PTFE−PMMA particles, which are close to spherical, we plot the calculated shell densities against a range of core diameters for every size of particle with trial values of D_{core} from 42 to 50 nm in Figure 1a.

Assuming the shell density does not significantly vary with the particle size, we evaluated the most probable particle core diameter by comparing the standard deviation in calculated shell densities with particle size for each trial core diameter. These deviations are plotted in Figure 1b against the trial value of D_{core}. The minimum deviation in ρ_{shell} across the different particles is observed for a core diameter of approximately 47 nm. Thus, using a core diameter of D_{core} = 47 nm and eq 4 gives a core density of ρ_{core} = 1.54 g/cm^3. This is approximately 80% of the bulk density of the employed PTFE[38] which is 1.95 g/cm^3. The lower than expected density could potentially be due to several factors. Porosity of the core would lead to a lower perceived density; however, STEM results (Figure 4) show no significant variation in the contrast at the core of the particles, which would be expected were this the case. A mixed PTFE−PMMA core could also result in the lower perceived density and would imply a core that is almost a 50/50 mix of the two materials. It is also possible that the nanoparticulate PTFE cores exhibit a reduced density due to lower crystallinity than bulk PTFE. Using the core diameter of 47 nm estimated here, and by subtracting this from the total particle dimensions measured using DLS, we can also estimate shell thicknesses, as given in Table 2 as T_{bulk}. It should be noted that as this method relies on the hydrodynamic size as measured by DLS to be used in the DCS calculations, which is larger than the "dry" value, this would be expected to underestimate the densities. However, given that the densities obtained for PMMA using a 47 nm core size (shown in Figure 1a) agree with the bulk density for atactic PMMA to within 2%, it is likely that the density reduction measured for the PTFE is similarly reliable.

Structural Analysis. Explicit information on fine structural details can only be acquired by use of analytical techniques sensitive to such features. It is important to ensure that any inconsistency between such measurements and the measurements performed using bulk analysis techniques are carefully interpreted and understood.

SEM measurements were used to visualize the surface morphology of the particles and to provide size measurements under dry, high-vacuum conditions. Particle diameters measured by SEM (D_{SEM}) are given in Table 3 together with the associated measurement uncertainties. A more detailed description of the error estimation for the size determination by SEM can be found elsewhere.[39]

When comparing the particle diameters measured by SEM to those measured by DLS, the SEM diameters are consistently smaller. For the cores, this discrepancy is small, between 1.6 and 3.6 nm; this is to be expected due to the hydrophobic nature of the PTFE cores. For the PTFE−PS particles, the difference ranges from 6.8 to 12.1 nm. For the PTFE−PMMA particles, the difference ranges from 7.7 nm to 16.2 nm. Not all this discrepancy can be explained by the difference between the hydrodynamic and "dry" particle sizes. It is possible that the disparity can be explained by underestimation of the particle size in SEM due to beam damage of the particles. The difference in diameter between DLS and SEM measurements is notably greater for the PMMA-coated particles, which may be partially explained by a combination of swelling of the PMMA due to absorbed water,[40] and the difference in hydrophilicity of the materials resulting in a larger hydrodynamic diameter for the PMMA-coated particles with respect to the PS-coated particles. A more significant factor in this difference in behavior may be due to the PMMA shell shrinking under electron irradiation; PMMA is a well-known positive photoresist for both photolithography and electron beam lithography.[41] Conversely, PS is a negative photoresist and can be expected to be more dimensionally stable under electron beam irradiation.[42] It is also possible that the larger sizes are due to polydispersity in the nanoparticle populations, possibly as a result of low levels of aggregates. However, the DCS analysis shows that this is not a likely explanation.

Table 3. Particle Diameters Measured by SEM (D_{SEM}) Together with Associated Measurement Uncertainties, and the Difference to the DLS-Determined Values $\Delta D_{(\text{DLS−SEM})}$

sample	D_{SEM}	$\Delta D_{(\text{DLS−SEM})}$
cores	45.4 ± 10.4	1.6/3.6[a]
PTFE−PS(1)	53.2 ± 10.2	9.9
PTFE−PS(2)	64.1 ± 8.4	7.0
PTFE−PS(3)	77.6 ± 7.2	6.8
PTFE−PS(4)	88.5 ± 6.8	9.5
PTFE−PS(5)	109.9 ± 4.9	10.1
PTFE−PS(6)	146.9 ± 4.7	12.1
PTFE−PMMA(1)	60.4 ± 9.0	12.4
PTFE−PMMA(2)	86.0 ± 9.6	7.7
PTFE−PMMA(3)	112.9 ± 6.6	9.8
PTFE−PMMA(4)	143.8 ± 10.6	16.2

[a]The two values reported for the cores represent the direct DLS value, and the estimate provided by combination with DCS and TGA data for all particles.

SEM measurements of the PTFE−PS particles in transmission mode highlighted the incomplete shell coverage, as depicted in Figure 2. The different reactions of PMMA and PS to electron irradiation have been discussed in the literature for a long time. Scission of the polymer chains into smaller molecules is the primary process occurring in PMMA, whereas in PS, cross-link formation between the polymer chains is predominant.[41,43−45] It is notable that the diameters measured by SEM are less than those measured by DLS (given in Table 2)—for the PTFE−PS particles, this difference is typically within the amount expected due to the difference between hydrodynamic and "dry" diameters. For the PTFE−PMMA particles, however, this difference is considerably larger. This is likely due to the higher sensitivity of PMMA to electron-beam damage resulting in degradation.

For the PTFE−PS particles, coverage of the shell around the cores appears incomplete at low shell thickness but appears to increase with the increasing particle size. Further SEM

https://dx.doi.org/10.1021/acs.jpcc.0c02161
J. Phys. Chem. C 2020, 124, 11200−11211

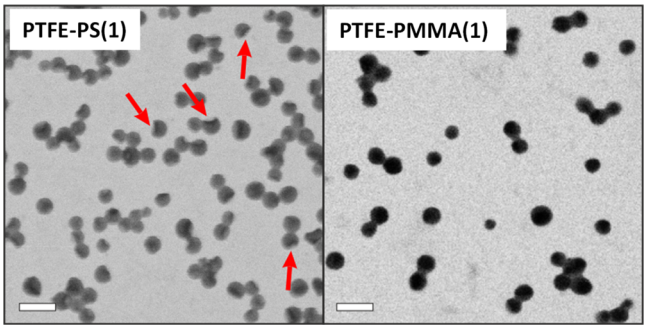

Figure 2. SEM micrographs recorded in transmission mode of the samples PTFE−PS(1) and PTFE−PMMA(3). Red arrows indicate some of the most obvious examples of the Hyflon core being exposed by the PS shell. Both scale bars equal 100 nm.

micrographs of the particles can be found in the Supporting Information (Figure S3).

SEM micrographs of uncoated particles from samples PTFE−PS(3), PTFE−PS(4), PTFE−PS(5), and PTFE−PS(6) were used to measure the incomplete shell coverage observed on their surfaces. At least 25 particles were measured from each micrograph, and estimates were obtained for the proportion of particles with visibly incomplete shells and the average size of visible holes within the shell. Combined with the particle size measurements, the proportion of core which is uncoated could then be estimated. These measurements are reported in the Supporting Information in Table S2 and plotted in Figure 3.

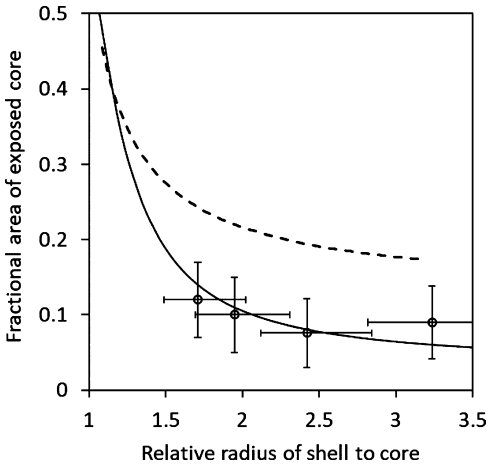

Figure 3. Relationship between the nonwetted area of the particle core to the ratio of the radii of the shell and the core material. The upper, dashed curve represents a core displaced 6 nm from the surface of the particle, as used for comparison in modeling of XPS intensities. The lower, solid line represents the predicted wetting model from theory, with a fixed 20° contact angle. Data extracted from SEM micrographs are shown as white circles. The error bars in relative radius relate to the core size dispersity, whereas those in the fractional area of exposed core reflect the range of measured sizes.

To compare the observed morphologies with the results of the interfacial energy calculations, we consider the case of a perfectly spherical, smooth, nondeformable core coated with a nonwetting liquid which has contact angle θ_E and no contact angle hysteresis. In this case, the equilibrium morphology consists of an area of nonwetted core and an area of wetted core (as opposed to the energetically less favorable case in which there are multiple separate areas of non-wetted core); thus, the shell is the relative complement of the core sphere in the shell sphere. This is indicated in Scheme 1A and represents the case of the PS-coated particles in water. The fact that we observe the nonwetting area as a hollow in SEM is somewhat surprising, but this may be attributed to the shrinking of the core, which is either a result of the lower than expected density, which is detailed previously, or the electron beam interaction with these materials. PS is known to cross-link under electron beam radiation, whereas PTFE has a removal rate similar to that of PMMA.[46] Shrinkage of the core will cause a hollow to form in the nonwetting area as indicated in Scheme 1B. The size of nonwetted area in Scheme 1A can be calculated by trigonometry, using the radius of the outer shell surface, the radius of the core and the defined contact angle. The fractional area of the core that is exposed should tend toward a constant value: that of a spherical particle of PTFE at the surface of a flat PS sample. In the case of a 20° contact angle, the fractional area in that case is 3% of the PTFE surface exposed. As the amount of PS decreases, a larger surface area should be exposed; the curve describing the ideal relationship for a 20° contact angle is shown in Figure 3 along with data extracted from the SEM images as points. It should be noted that measurements made from SEM images of the hole in the shell do not necessarily directly represent the uncoated core area. The error bars on the points represent the range of sizes across the large number of individual particles.

The data from the SEM images provide, numerically, reasonable agreement with the model. However, the predicted reduction in the area fraction of core that is not wetted by PS as the amount of PS in the particle increases is not echoed in the data, where particles demonstrate a greater range of exposed areas within a population than between the different populations. This may partly be explained by the polydispersity of the core particles. Each population contains a range of relative ratios and it will only be the fraction of core particles that are large that will display a significantly larger "hole" in the SEM image. Indeed, it can be seen the range of exposed areas in a population increases with the reduced PS content. However, it is also likely that the irregular shape of the core particles causes contact line pinning, and this dominates over equilibrium considerations.

For the PTFE−PMMA particles which exhibit a complete coating, there remains uncertainty about the position of the core within the particle. From consideration of the surface energies of PMMA and PTFE in water, we would expect a complete shell; however, there is no requirement for the core to be central within this shell. STEM images of the PTFE−PMMA(1) particles taken in ABF and HAADF mode are shown in Figure 4 and clearly show the core−shell structure. It can be observed that the core of these particles is noncentral and possesses a significantly asymmetric shape. Shell thickness estimations from these images give results ranging from 3 to 17 nm, with estimated uncertainties of roughly 20%, with a minimum of 1 nm. The smaller structures visible within some of the images were identified as sulphurous deposits within the carbon layer of the TEM grids, attributed to residues from the manufacturing process. There was no evidence found of interaction between these structures and the nanoparticles. For the EDX measurements, particles that overlapped these deposits were avoided. As with SEM, the nanoparticles exhibited a high sensitivity to beam damage, with approximately 5 min of exposure to the beam causing damage to the

https://dx.doi.org/10.1021/acs.jpcc.0c02161
J. Phys. Chem. C 2020, 124, 11200−11211

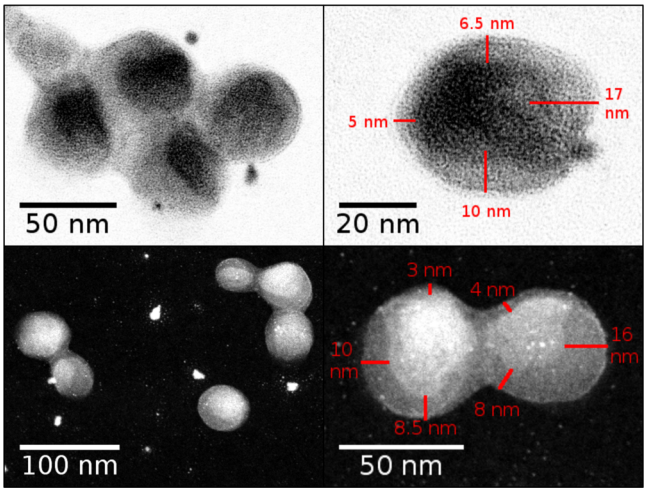

Figure 4. STEM images recorded in ABF mode (top) and HAADF mode (bottom) of sample PTFE−PMMA(1). Images have been edited for optimal contrast. Exemplary local shell thickness estimations are shown in the upper and lower right images.

point that the core−shell structure was no longer clearly observable and increasing the uncertainty of dimensional measurements.

An EDX line-scan of an individual particle (shown in the Supporting Information, Figure S4) showed distributions of oxygen and fluorine within the particle, confirming the core−shell structure and providing further evidence of the acentric core. The local core width and related uncertainty were estimated from this line scan at (35 ± 4) nm and the local particle width was estimated at (48 ± 6) nm, giving an average local shell thickness of ∼7 nm.

XPS provides quantitative information on the elemental and chemical composition of surfaces. The typical analysis volume for XPS is on the order of 10 nm in depth, and from 10 to ∼500 μm across, acting as a population measurement technique for nanoparticle samples. As such XPS measurements provide more statistically significant measurements to support observations made using techniques such as SEM and STEM. The measurement of planar overlayer thicknesses from XPS data has been understood for some time.[47] More recently, developments have been made into the use of XPS to quantify thickness and composition of overlayers on nanoparticles,[20,32,48,49] either through empirical formulae[50,51] or by direct comparison to simulated data.[52,53] Some structural features cannot be easily distinguished by XPS peak analysis. Nanoparticles with an uneven coating or with defects, particles with off-center or diffuse cores, particle nonsphericity, and dispersity in populations will produce peak intensities which can be difficult to interpret accurately without prior knowledge.[54] In this work, the PTFE−PMMA series has a complete shell and the PTFE−PS series has an incomplete shell; therefore, it is instructive to evaluate the capability of XPS to distinguish these samples. Because of XPS being performed under vacuum, on samples that have been dried onto a substrate, the shell thicknesses measured would be expected to be closer to those determined by SEM than by solution-based techniques. In addition, it is important to highlight that due to the exponential attenuation of photoelectrons through material, for systems with a distribution of overlayer thicknesses the "average" value of the thickness as observed by XPS will tend toward a lower value than the true average.

Example survey and high-resolution C 1s spectra from samples PTFE−PMMA(1) and PTFE−PS(5) are shown in Figure 5. Inset figures within the survey spectra show the F 1s background region for each sample at 5× magnification,

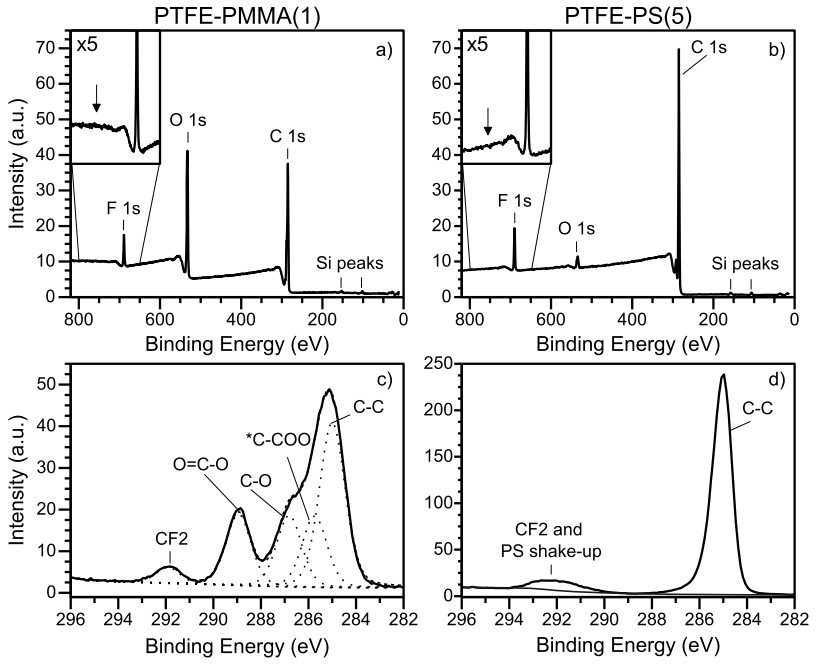

Figure 5. Representative XPS (a) survey spectrum for sample PTFE−PMMA(3) with inset showing F 1s background magnified 5× (b) survey spectrum for sample PTFE−PS(7) with inset showing F 1s background magnified 5× (c) C 1s high-resolution spectrum for sample PTFE−PMMA(3) (* is used to indicate the relevant carbon atom relating to a secondary energy shift) and (d) C 1s high-resolution spectrum for sample PTFE−PS(7).

https://dx.doi.org/10.1021/acs.jpcc.0c02161
J. Phys. Chem. C 2020, 124, 11200−11211

highlighting differing background shapes. These two samples are shown due to their similar F 1s peak intensity, despite significant differences in the structure and amount of shell material present. The C 1s spectra for samples PTFE−PMMA(1) and PTFE−PS(5) depict the characteristic PMMA and PS peak structures, with the addition of a peak corresponding to carbon ($-CF_2-$) in PTFE, at a binding energy of approximately 292 eV.

Under the assumption of a uniform core−shell structure, the average nanoparticle shell thickness can be estimated using empirical formulae such as in the T_{NP} method.[50] However, there are currently no such straightforward methods of analysis that can be applied to nonideal structures such as those seen here.

In order to interpret the XPS data, we use the information provided by the combination of TGA, DLS, and DCS, indicating that the core of the particles is less dense than bulk PTFE. As discussed previously, this may be simply due to a reduced crystallinity in comparison to the bulk material resulting in a lower density pure PTFE core, or it may indicate mixing of the shell material into the core. To estimate expected peak intensities from these particles, modeling was performed using a simple computer script, similar to those used in previous work,[49−51] across a range of particle dimensions and orientations. Intensities for individual columns of material within a particle are calculated and summed across the entire volume of the particle. The ratios of these summed intensities are thus equivalent to the expected intensity ratios that would be measured from a single particle. The average intensity ratios obtained across the range of particle orientations modeled is therefore equivalent to those for a population of randomly deposited particles.[55] Intensities for elements within the shell ($I_{x(\text{shell})}$) from a single column of material were calculated using eq 6, where I_{pure} is the intensity measured for a sample of a pure, flat, bulk reference material (all of which were measured using the same instrument with the same settings); $L_{x,y}$ is the effective attenuation length of electrons of a photoelectron peak from element x through material y, as calculated using the formula described by Seah;[56] a_1 and a_2 are the thicknesses of the shell material within the column above and below the core material respectively; and b is the thickness of the core material in the column. Intensities for elements within the core ($I_{x(\text{core})}$) were calculated using eq 7, in which all terms retain their meaning. Details of the geometry calculations involved in determining the dimensions of each column can be found in the Supporting Information.

$$I_{x(\text{shell})} = I_{x(\text{pure})}[1 - e^{(-a_1/L_{x,\text{shell}})}(1 - e^{(-b/L_{x,\text{core}})}(1 - e^{(-a_2/L_{x,\text{shell}})}))] \quad (6)$$

$$I_{x(\text{core})} = I_{x(\text{pure})}\, e^{(-a_1/L_{x,\text{shell}})}(1 - e^{(-b/L_{x,\text{core}})}) \quad (7)$$

To account for the density difference compared to bulk material, the pure reference intensities were multiplied by the fractional density relative to bulk values, and the value of the effective attenuation lengths were similarly adjusted. A small (sub-monolayer) amount of carbon contamination was included in the model to minimize deviation between calculated thicknesses determined using the signal arising from carbon and oxygen in the shell.

For the larger PTFE−PMMA-series particles, slightly higher F 1s intensities were measured than would be expected for a particle with a complete shell and centralized core. This is consistent with the off-center cores observed in the STEM. To consider the effect on the expected XPS intensities, a displacement of the core was implemented into the script. A range of both fractional and absolute displacements were modeled for a large range of shell thicknesses. The calculated F 1s peak intensities (corrected for instrument transmission and peak sensitivity factor) for ideal and displaced core models are given alongside experimentally determined values in Figure 6, and the models are depicted in Scheme 1.

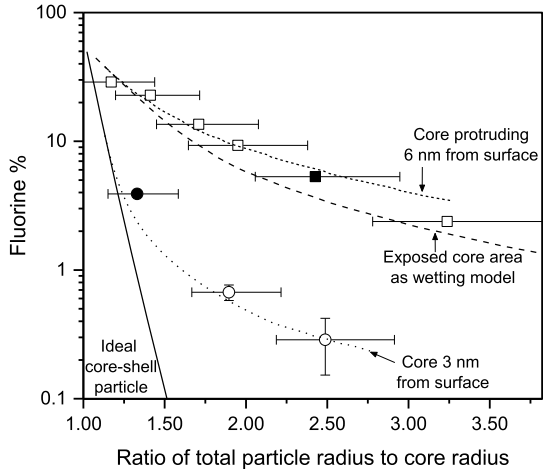

Figure 6. Observed F 1s intensity as a percentage of total XPS peak intensity for both PTFE−PS (□) and PTFE−PMMA (○) particles, alongside modeling data for a selection of potential structures, assuming a reduced-density core. The solid line represents particles with a uniform concentric shell; the dotted line represents particles with a core displaced such that its surface is 3 nm from the shell surface; and the dashed lines represent particles in which the core protrudes from the shell either by a fixed 6 nm (chosen as it gives reasonable agreement with the data), or by an amount determined from the exposed core surface area predicted from the wetting model. For protruding core models, the "total particle radius" used is that of a volume equivalent sphere. The shaded points indicate data from the spectra shown in Figure 5. x-axis errors represent the variability within the population due to the size distribution of the core particles, while y-axis errors represent the uncertainty in the measured peak areas. Where not visible, error bars for the observed intensities are smaller than the data marker.

These intensities are plotted against the ratio between the total size of each particle as determined from SEM to the size of the core. The observed fluorine intensities indicate a considerable displacement of the core for the PTFE−PMMA particles. The trend observed matches well with a model in which the cores are displaced such that the surface of the core is around 3 nm from the surface of the particles. For variable displacement across the particle population, this would indicate an average displacement of slightly greater than 3 nm, due to the exponential attenuation of the electron signal resulting in a bias toward underestimation of the thickness. The dashed lines in Figure 6 correspond to a model for the PTFE−PS particles in which the core is protruding from a sphere of the shell material by either 6 nm or a distance determined by the expected exposed core surface-area from wettability calculations. The line corresponding to a protrusion of 6 nm provides greatest average agreement with the experimental data; however, this still does not fully explain

https://dx.doi.org/10.1021/acs.jpcc.0c02161
J. Phys. Chem. C 2020, 124, 11200−11211

the measured intensities. The exposed-core surface-area fraction corresponding to these models is plotted on Figure 3.

Because of the surface-sensitivity of XPS, thickness determination using peak intensity analysis can typically only be performed for particles with a shell thickness of the order of 10 nm or less. However, greater information on the structure of a given sample can be obtained by considering the shape of the background signal. As the background consists primarily of inelastically scattered electrons, the background shape at binding energies immediately above a given peak can reveal the presence, or lack, of an overlayer material. This is apparent here in the magnified inset of the survey spectra for PTFE−PMMA(1) and PTFE−PS(5) given in Figure 5, where the background above the F 1s peak exhibits differing behavior between the two samples. The slight rise visible for PTFE−PMMA(1) indicates the presence of an overlayer of a different material, while the typical exponential decay in signal observed for PTFE−PS(5) is closer to that expected for bulk material. This indicates that the PTFE−PS particles have a significant fraction of uncovered core material and are thus not of an ideal core−shell morphology.

Such observations can typically only provide qualitative indications of a sample's structure; however, methods of empirically fitting the XPS background[57] can allow more quantitative interpretation and potentially fitting of entire XPS survey spectra. The method described by Shard and Spencer[57] allows fitting of backgrounds for simple planar overlayer systems; with some modification, as shown in Scheme 2, we can also use this method to approximate nanoparticles.

Scheme 2. Illustrative Schematic of the Adaptations Made to the Planar Overlayer Model[57] to Approximate Nanoparticles with and without Complete Shell Coverage

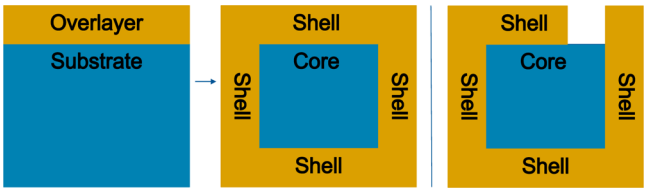

In this model, the signal contributions of four distinct portions of the particle are summed: the overlayer of shell material above the core; the 47 nm diameter core under the shell overlayer; the underlayer of shell material below the core; and the sides of pure shell material, with a depth equal to the diameter of the core plus twice the overlayer thickness. For sample PTFE−PS(5), an additional component representing a portion of the core with no overlayer was included, and the small O 1s signal from the substrate was accounted for within the fit as a separate, arbitrary amount of material. The width of the shell sides in this model was allowed to vary independently from the overlayer thickness, in order to compensate for factors such as nanoparticle topography, shell coverage, and core displacement. Prior to fitting, a small amount of background due to signal arising from the silicon substrate was removed by fitting an exponential decay to the slope of the background above the silicon peaks. As we do not consider the curvature of the particles in the axis of the analyzer, a bias toward underestimation of the overlayer will be introduced. Likewise, with no curvature, we also do not consider the contribution of particles beneath the top layer, which may be shadowed by the edges of the top layer of nanoparticles; thus, another bias will be introduced toward an overestimation of the overlayer thickness. Combined with the high number of variables used in the modeling of the background, the results may be considered to lend support where consistent with other measurements but should not be interpreted as direct measurements. A more complex modeling of such particles is possible but would require careful consideration with regard to both sample preparation and the model used and is beyond the scope of this paper.

Fitting was performed using initial values for dimensions based on those obtained from the SEM and background intensity factors based on those observed for pure material references. Example fits for samples PTFE−PMMA(1) and PTFE−PS(5) are given in Figure 7. These samples are shown due to their similar fluorine 1s peak intensities, despite distinct differences in structure which can be inferred from the XPS background. For the PTFE−PMMA(1) fit, an overlayer thickness of 4.8 nm was obtained, reasonably close to that estimated through peak analysis. For PTFE−PS(5), a good fit could be obtained with arbitrarily large overlayer thicknesses, with the F 1s peak and background intensity arising predominantly from the uncovered core area, and the background shape across the spectrum being approximately equivalent to a mixture of the bulk materials. As such, this type of modeling is unsuited to nanoparticle systems with significant gaps in the coating layer—these can be visually identified by the background shape as described previously.

CONCLUSIONS

We have demonstrated that the formation of nonstandard core−shell nanoparticle morphologies by use of emulsion polymerization can be predicted by consideration of the appropriate interfacial energies of the system, allowing shell coverage to be estimated. In this manner, specific nanoparticle morphologies with tailored coating coverages may be created. The characterization of such systems, while challenging, can be consistently achieved using a careful selection of complementary analytical techniques. A combination of bulk analysis techniques such as TGA, DLS, and DCS may be used to identify the amount of material present and infer information regarding density. Imaging techniques such as SEM and STEM may be used to identify external and, with some effort, internal morphology, respectively. With the information provided by other techniques, it was possible to use XPS alongside numerical modeling to determine an estimate of the typical effective core-displacement of the PMMA-coated particles, which was consistent with the coating asymmetry observed by STEM. Modeling of the PTFE−PS particles as a system with a protruding core provided reasonable agreement with the observed XPS intensities; however, precise agreement could not be achieved with either a fixed displacement model or a wettability-based model. The importance of careful inspection of the XPS inelastic background in spectra from samples of unknown morphology was demonstrated, as it can be used to immediately identify the non-core−shell nature of the PTFE−PS particles. Rudimentary modeling of the inelastic background was performed, demonstrating that such methods may reasonably be used to lend support to overlayer thickness measurements for coated nanoparticles, but not for those in which the coating is incomplete. Distinct differences between size and overlayer thickness estimates from different techniques, particularly in comparison between solution-based and ultrahigh vacuum-based techniques, were observed

https://dx.doi.org/10.1021/acs.jpcc.0c02161
J. Phys. Chem. C 2020, 124, 11200−11211

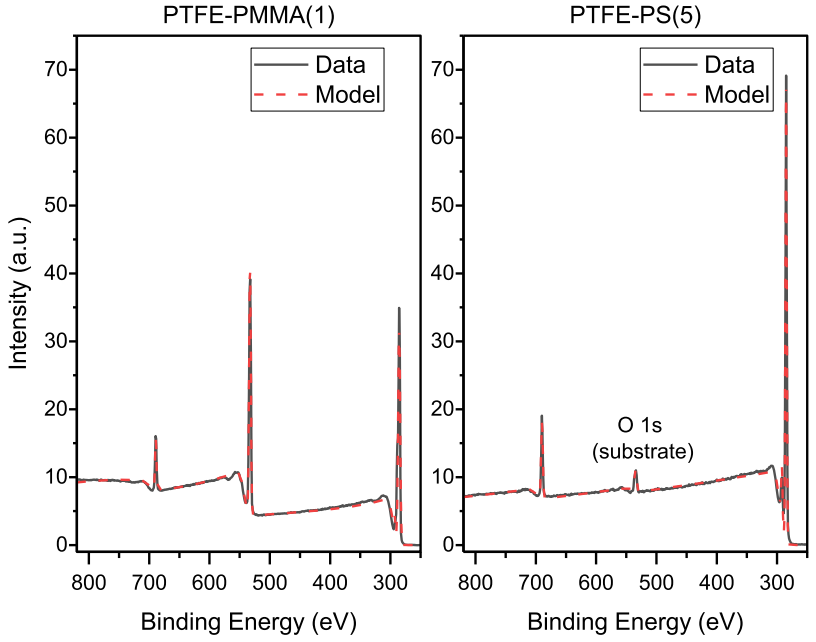

Figure 7. Survey spectra fits for samples PTFE−PMMA(1) and PTFE−PS(5). A small amount of oxygen is visible in the spectrum for PTFE−PS(5), arising from the oxide layer on the silicon substrate.

and potential explanations of these discrepancies were provided.

■ ASSOCIATED CONTENT

Supporting Information

The Supporting Information is available free of charge at https://pubs.acs.org/doi/10.1021/acs.jpcc.0c02161.

Interfacial energies used in wetting calculations; TGA curves for all particles; DCS size distributions for all particles (excluding uncoated cores); additional SEM micrographs; SEM measurements of "holes" in the PS coatings; EDX line scan and spectra of a PMMA-coated particle; detailed description of the XPS peak intensity modeling; and parameters used for the XPS background fit (PDF)

■ AUTHOR INFORMATION

Corresponding Author

David J. H. Cant − *Chemical and Biological Sciences, National Physical Laboratory (NPL), Teddington, Middlesex TW11 0LW, United Kingdom;* orcid.org/0000-0002-4247-5739; Email: david.cant@npl.co.uk

Authors

Caterina Minelli − *Chemical and Biological Sciences, National Physical Laboratory (NPL), Teddington, Middlesex TW11 0LW, United Kingdom;* orcid.org/0000-0002-8092-251X

Katia Sparnacci − *Dipartimento di Scienze dell' Ambiente e della Vita, Università del Piemonte Orientale "A. Avogadro", 15100 Alessandria, Italy*

Anja Müller − *Division 6.1 Surface Analysis and Interfacial Chemistry, Bundesanstalt für Materialforschung und-prüfung (BAM), 12203 Berlin, Germany;* orcid.org/0000-0003-2085-3687

Henryk Kalbe − *Institute of Applied Physics, Vienna University of Technology, 1040 Wien, Austria*

Michael Stöger-Pollach − *University Service Center for TEM, Vienna University of Technology, 1040 Wien, Austria*

Wolfgang E. S. Unger − *Division 6.1 Surface Analysis and Interfacial Chemistry, Bundesanstalt für Materialforschung und-prüfung (BAM), 12203 Berlin, Germany;* orcid.org/0000-0002-7670-4042

Wolfgang S. M. Werner − *Institute of Applied Physics, Vienna University of Technology, 1040 Wien, Austria;* orcid.org/0000-0002-4870-9137

Alexander G. Shard − *Chemical and Biological Sciences, National Physical Laboratory (NPL), Teddington, Middlesex TW11 0LW, United Kingdom*

Complete contact information is available at: https://pubs.acs.org/10.1021/acs.jpcc.0c02161

Notes

The authors declare no competing financial interest.

■ ACKNOWLEDGMENTS

This work was funded by project 14IND12 Innanopart of the EMPIR programme co-financed by the Participating States, from the European Union's Horizon 2020 research and innovation program, and the National Measurement System of the UK Department of Business, Energy and Industrial Strategy (BEIS). The authors thank Sigrid Benemann (Division 6.1, BAM, Germany) for recording the micrographs at the Supra 40 SEM, and Michael Krumrey and his team at the Physikalisch-Technische Bundesanstalt (PTB) for their assistance in characterizing these nanoparticle systems.

■ REFERENCES

(1) Jain, P. K.; El Sayed, I. H.; El-Sayed, M. A. Au Nanoparticles Target Cancer. *Nano Today*; Elsevier, 2007; pp 18−29.

(2) Ferrari, M. Cancer Nanotechnology: Opportunities and Challenges. *Nat. Rev. Cancer* **2005**, *5*, 161−171.

(3) Ambrosi, A.; Airò, F.; Merkoçi, A. Enhanced Gold Nanoparticle Based ELISA for a Breast Cancer Biomarker. *Anal. Chem.* **2010**, *82*, 1151−1156.

(4) Wang, Y.; Gao, S.; Ye, W.-H.; Yoon, H. S.; Yang, Y.-Y. Co-Delivery of Drugs and DNA from Cationic Core-Shell Nanoparticles Self-Assembled from a Biodegradable Copolymer. *Nat. Mater.* **2006**, *5*, 791−796.
(5) Minelli, C.; Lowe, S. B.; Stevens, M. M. Engineering Nanocomposite Materials for Cancer Therapy. *Small* **2010**, *6*, 2336−2357.
(6) Witte, P. T.; Berben, P. H.; Boland, S.; Boymans, E. H.; Vogt, D.; Geus, J. W.; Donkervoort, J. G. BASF NanoSelect Technology: Innovative Supported Pd- and Pt-based Catalysts for Selective Hydrogenation Reactions. *Top Catal* **2012**, *55*, 505.
(7) Hensel, J.; Wang, G.; Li, Y.; Zhang, J. Z. Synergistic Effect of CdSe Quantum Dot Sensitization and Nitrogen Doping of TiO2 Nanostructures for Photoelectrochemical Solar Hydrogen Generation. *Nano Lett.* **2010**, *10*, 478−483.
(8) Zhu, H.; Song, N.; Lian, T. Controlling Charge Separation and Recombination Rates in CdSe/ZnS Type I Core−Shell Quantum Dots by Shell Thicknesses. *J. Am. Chem. Soc.* **2010**, *132*, 15038−15045.
(9) Hardman, S. J. O.; Graham, D. M.; Stubbs, S. K.; Spencer, B. F.; Seddon, E. A.; Fung, H.-T.; Gardonio, S.; Sirotti, F.; Silly, M. G.; Akhtar, J.; et al. Electronic and Surface Properties of PbS Nanoparticles Exhibiting Efficient Multiple Exciton Generation. *Phys. Chem. Chem. Phys.* **2011**, *13*, 20275−20283.
(10) Knight, M. W.; Halas, N. J. Nanoshells to Nanoeggs to Nanocups: Optical Properties of Reduced Symmetry Core−Shell Nanoparticles beyond the Quasistatic Limit. *New J. Phys.* **2008**, *10*, 105006.
(11) Xu, X.; Rosi, N. L.; Wang, Y.; Huo, F.; Mirkin, C. A. Asymmetric Functionalization of Gold Nanoparticles with Oligonucleotides. *J. Am. Chem. Soc.* **2006**, *128*, 9286−9287.
(12) Gutiérrez, L.; Costo, R.; Grüttner, C.; Westphal, F.; Gehrke, N.; Heinke, D.; Fornara, A.; Pankhurst, Q. A.; Johansson, C.; Veintemillas-Verdaguer, S.; Morales, M. P. Synthesis Methods to Prepare Single- and Multi-Core Iron Oxide Nanoparticles for Biomedical Applications. *Dalton Trans.* **2015**, *44*, 2943−2952.
(13) Langlois, C.; Li, Z. L.; Yuan, J.; Alloyeau, D.; Nelayah, J.; Bochicchio, D.; Ferrando, R.; Ricolleau, C. Transition from core-shell to Janus chemical configuration for bimetallic nanoparticles. *Nanoscale* **2012**, *4*, 3381.
(14) Perro, A.; Meunier, F.; Schmitt, V.; Ravaine, S. Production of Large Quantities of "Janus" Nanoparticles Using Wax-in-Water Emulsions. *Colloids Surf., A* **2009**, *332*, 57−62.
(15) Alexeev, A.; Uspal, W. E.; Balazs, A. C. Harnessing Janus Nanoparticles to Create Controllable Pores in Membranes. *ACS Nano* **2008**, *2*, 1117−1122.
(16) Bell, N. C.; Minelli, C.; Tompkins, J.; Stevens, M. M.; Shard, A. G. Emerging Techniques for Submicrometer Particle Sizing Applied to Stöber Silica. *Langmuir* **2012**, *28*, 10860−10872.
(17) Gollwitzer, C.; Bartczak, D.; Goenaga-Infante, H.; Kestens, V.; Krumrey, M.; Minelli, C.; Pálmai, M.; Ramaye, Y.; Roebben, G.; Sikora, A.; et al. Comparison of Techniques for Size Measurement of Nanoparticles in Cell Culture Medium. *Anal. Methods* **2016**, *8*, 5272−5282.
(18) Minelli, C.; Sikora, A.; Garcia-Diez, R.; Sparnacci, K.; Gollwitzer, C.; Krumrey, M.; Shard, A. G. Measuring the Size and Density of Nanoparticles by Centrifugal Sedimentation and Flotation. *Anal. Methods* **2018**, *10*, 1725−1732.
(19) Sikora, A.; Bartczak, D.; Geißler, D.; Kestens, V.; Roebben, G.; Ramaye, Y.; Varga, Z.; Palmai, M.; Shard, A. G.; Goenaga-Infante, H.; et al. A Systematic Comparison of Different Techniques to Determine the Zeta Potential of Silica Nanoparticles in Biological Medium. *Anal. Methods* **2015**, *7*, 9835−9843.
(20) Belsey, N. A.; Shard, A. G.; Minelli, C. Analysis of Protein Coatings on Gold Nanoparticles by XPS and Liquid-Based Particle Sizing Techniques. *Biointerphases* **2015**, *10*, 019012.
(21) Baer, D. R.; Engelhard, M. H.; Johnson, G. E.; Laskin, J.; Lai, J.; Mueller, K.; Munusamy, P.; Thevuthasan, S.; Wang, H.; Washton, N.; et al. Surface Characterization of Nanomaterials and Nanoparticles: Important Needs and Challenging Opportunities. *J. Vac. Sci. Technol., A* **2013**, *31*, 050820.
(22) Cressey, D. Tiny Traits Cause Big Headaches. *Nature* **2010**, *467*, 264−265.
(23) Baer, D. R.; Amonette, J. E.; Sarathy, V.; Wang, C.-M.; Sharma, A.; Gaspar, D. J.; Seal, S.; Nachimuthu, P.; Nurmi, J. T.; Kuchibhatla, S.; Qiang, Y.; et al. Characterization Challenges for Nanomaterials. *Surf. Interface Anal.* **2008**, *40*, 529−537.
(24) Nisisako, T.; Torii, T. Formation of Biphasic Janus Droplets in a Microfabricated Channel for the Synthesis of Shape-Controlled Polymer Microparticles. *Adv. Mater.* **2007**, *19*, 1489−1493.
(25) Giani, E.; Sparnacci, K.; Laus, M.; Palamone, G.; Kapelioushko, V.; Arcella, V. PTFE−Polystyrene Core−Shell Nanospheres and Nanocomposites. *Macromolecules* **2003**, *36*, 4360−4367.
(26) Mie, G. Beiträge zur Optik trüber Medien, speziell kolloidaler Metallösungen. *Ann. Phys.* **1908**, *330*, 377−445.
(27) Stetefeld, J.; McKenna, S. A.; Patel, T. R. Dynamic Light Scattering: A Practical Guide and Applications in Biomedical Sciences. *Biophys. Rev.* **2016**, *8*, 409−427.
(28) Miller, C. C. The Stokes-Einstein Law for Diffusion in Solution. *Proc. R. Soc. A* **1924**, *106*, 724−749.
(29) Rades, S.; Hodoroaba, V.-D.; Salge, T.; Wirth, T.; Lobera, M. P.; Labrador, R. H.; Natte, K.; Behnke, T.; Gross, T.; Unger, W. E. S. High-Resolution Imaging with SEM/T-SEM, EDX and SAM as a Combined Methodical Approach for Morphological and Elemental Analyses of Single Engineered Nanoparticles. *RSC Adv.* **2014**, *4*, 49577−49587.
(30) Schneider, C. A.; Rasband, W. S.; Eliceiri, K. W. NIH Image to ImageJ: 25 Years of Image Analysis. *Nat. Methods* **2012**, *9*, 671−675.
(31) Gatan, Inc. http://www.gatan.com/(accessed Feb 27, 2018).
(32) Belsey, N. A.; Cant, D. J. H.; Minelli, C.; Araujo, J. R.; Bock, B.; Brüner, P.; Castner, D. G.; Ceccone, G.; Counsell, J. D. P.; Dietrich, P. M.; et al. Versailles Project on Advanced Materials and Standards Interlaboratory Study on Measuring the Thickness and Chemistry of Nanoparticle Coatings Using XPS and LEIS. *J. Phys. Chem. C* **2016**, *120*, 24070−24079.
(33) Good, R. J.; Girifalco, L. A. A Theory for Estimation of Surface and Interfacial Energies. III. Estimation of Surface Energies of Solids from Contact Angle Data. *J. Phys. Chem.* **1960**, *64*, 561−565.
(34) Carré, A. Polar Interactions at Liquid/Polymer Interfaces. *J. Adhes. Sci. Technol.* **2007**, *21*, 961−981.
(35) Ellison, A. H.; Zisman, W. A. Wettability of Halogenated Organic Solid Surfaces. *J. Phys. Chem.* **1954**, *58*, 260−265.
(36) de Gennes, P.-G.; Brochard-Wyart, F.; Quéré, D. *Capillarity and Wetting Phenomena*; Springer: New York, 2004.
(37) Mark, J. E. *Physical Properties of Polymers Handbook*; Mark, J. E., Ed.; Springer New York: New York, 2007.
(38) Hyflon PFA & MFA—Technical Data Sheets. Solvay https://www.solvay.com/en/brands/hyflon-pfa-mfa/technical-data-sheets (accessed April 26, 2020).
(39) Müller, A.; Heinrich, T.; Tougaard, S.; Werner, W. S. M.; Hronek, M.; Kunz, V.; Radnik, J.; Stockmann, J. M.; Hodoroaba, V.-D.; Benemann, S.; et al. Determining the Thickness and Completeness of the Shell of Polymer Core-Shell Nanoparticles by X-ray Photoelectron Spectroscopy, Secondary Ion Mass Spectrometry, and Transmission Scanning Electron Microscopy. *J. Phys. Chem. C* **2019**, *123*, 29765.
(40) N'Diaye, M.; Pascaretti-Grizon, F.; Massin, P.; Baslé, M. F.; Chappard, D. Water Absorption of Poly(Methyl Methacrylate) Measured by Vertical Interference Microscopy. *Langmuir* **2012**, *28*, 11609−11614.
(41) Tiwari, P.; Srivastava, A. K.; Khattak, B. Q.; Verma, S.; Upadhyay, A.; Sinha, A. K.; Ganguli, T.; Lodha, G. S.; Deb, S. K. Structural Modification of Poly (Methyl Methacrylate) Due to Electron Irradiation. *Measurement* **2014**, *51*, 1−8.
(42) Ma, S.; Con, C.; Yavuz, M.; Cui, B. Polystyrene Negative Resist for High-Resolution Electron Beam Lithography. *Nanoscale Res. Lett.* **2011**, *6*, 446.

https://dx.doi.org/10.1021/acs.jpcc.0c02161
J. Phys. Chem. C 2020, 124, 11200−11211

(43) Stenn, K.; Bahr, G. F. Specimen Damage Caused by the Beam of the Transmission Electron Microscope, a Correlative Reconsideration. *J. Ultrastruct. Res.* **1970**, *31*, 526−550.
(44) Ditchfield, R. W.; Grubb, D. T.; Whelan, M. J. Electron Energy Loss Studies of Polymers during Radiation Damage. *Philos. Mag.* **1973**, *27*, 1267−1280.
(45) Grubb, D. T. Radiation Damage and Electron Microscopy of Organic Polymers. *J. Mater. Sci.* **1974**, *9*, 1715−1736.
(46) Karre, V. Direct Electron-Beam Patterning of Teflon-AF and Its Application to Optical Waveguiding. MS Thesis, University of Kentucky, 2009.
(47) Cumpson, P. J. The Thickogram: A Method for Easy Film Thickness Measurement in XPS. *Surf. Interface Anal.* **2000**, *29*, 403−406.
(48) Shard, A. G.; Wang, J.; Spencer, S. J. XPS Topofactors: Determining Overlayer Thickness on Particles and Fibres. *Surf. Interface Anal.* **2009**, *41*, 541−548.
(49) Kalbe, H.; Rades, S.; Unger, W. E. S. Determining Shell Thicknesses in Stabilised CdSe@ZnS Core-Shell Nanoparticles by Quantitative XPS Analysis Using an Infinitesimal Columns Model. *J. Electron Spectrosc. Relat. Phenom.* **2016**, *212*, 34−43.
(50) Shard, A. G. A Straightforward Method For Interpreting XPS Data From Core-Shell Nanoparticles. *J. Phys. Chem. C* **2012**, *116*, 16806−16813.
(51) Cant, D. J. H.; Wang, Y.-C.; Castner, D. G.; Shard, A. G. A Technique for Calculation of Shell Thicknesses for Core-Shell-Shell Nanoparticles from XPS Data. *Surf. Interface Anal.* **2016**, *48*, 274−282.
(52) Smekal, W.; Werner, W. S. M.; Powell, C. J. Simulation of Electron Spectra for Surface Analysis (SESSA): A Novel Software Tool for Quantitative Auger-Electron Spectroscopy and X-Ray Photoelectron Spectroscopy. *Surf. Interface Anal.* **2005**, *37*, 1059−1067.
(53) Chudzicki, M.; Werner, W. S. M.; Shard, A. G.; Wang, Y.-C.; Castner, D. G.; Powell, C. J. Evaluating the Internal Structure of Core-Shell Nanoparticles Using X-Ray Photoelectron Intensities and Simulated Spectra. *J. Phys. Chem. C* **2015**, *119*, 17687−17696.
(54) Wang, Y.-C.; Engelhard, M. H.; Baer, D. R.; Castner, D. G. Quantifying the Impact of Nanoparticle Coatings and Nonuniformities on XPS Analysis: Gold/Silver Core-Shell Nanoparticles. *Anal. Chem.* **2016**, *88*, 3917−3925.
(55) Werner, W. S. M.; Chudzicki, M.; Smekal, W.; Powell, C. J. Interpretation of Nanoparticle X-Ray Photoelectron Intensities. *Appl. Phys. Lett.* **2014**, *104*, 243106.
(56) Seah, M. P. Simple Universal Curve for the Energy-Dependent Electron Attenuation Length for All Materials. *Surf. Interface Anal.* **2012**, *44*, 1353−1359.
(57) Shard, A. G.; Spencer, S. J. A Simple Approach to Measuring Thick Organic Films Using the XPS Inelastic Background. *Surf. Interface Anal.* **2017**, *49*, 1256−1270.

https://dx.doi.org/10.1021/acs.jpcc.0c02161
J. Phys. Chem. C 2020, 124, 11200−11211